

Compactly Supported Radial Basis Functions Based Collocation Method for Level-Set Evolution in Image Segmentation

Arnaud Gelas, *Member, IEEE*, Olivier Bernard, Denis Friboulet, *Member, IEEE*, and Rémy Prost, *Member, IEEE*

Abstract—The partial differential equation driving level-set evolution in segmentation is usually solved using finite differences schemes. In this paper, we propose an alternative scheme based on radial basis functions (RBFs) collocation. This approach provides a continuous representation of both the implicit function and its zero level set. We show that compactly supported RBFs (CSRBFs) are particularly well suited to collocation in the framework of segmentation. In addition, CSRBFs allow us to reduce the computation cost using a *kd*-tree-based strategy for neighborhood representation. Moreover, we show that the usual reinitialization step of the level set may be avoided by simply constraining the l_1 -norm of the CSRBF parameters. As a consequence, the final solution is topologically more flexible, and may develop new contours (i.e., new zero-level components), which are difficult to obtain using reinitialization. The behavior of this approach is evaluated from numerical simulations and from medical data of various kinds, such as 3-D CT bone images and echocardiographic ultrasound images.

Index Terms—Active contours, collocation, deformable models, level sets, partial differential equations (PDEs), radial basis functions (RBFs), segmentation.

I. INTRODUCTION

SINCE its introduction in 1987 [1], *level-set* formulations have become a well-established and popular tool in the field of image processing, as shown by recent surveys [2]–[4]. In image segmentation, level-set-based methods can be seen as a class of deformable models, where the shape to be recovered is captured by propagating an interface represented by the zero level set of a smooth function (usually called the *level-set function*). Formally, the evolution of the interface is driven by a time-dependent partial differential equation (PDE) where the so-called velocity term reflects the image features characterizing the object to be segmented.

Manuscript received August 23, 2006; revised February 12, 2006. This work was supported in part by the Cluster project I3M: *Imagerie Médicale et Modélisations Multiéchelles: du petit animal à l'Homme* and in part by the *Fondation pour la Recherche Médicale* scholarship. This work is within the scope of the scientific topics of the PRC-GDR ISIS research group of the French National Center for Scientific Research (CNRS). The associate editor coordinating the review of this manuscript and approving it for publication was Prof. Vicent Caselles.

The authors are with the CREATIS-LRMN, INSA, UCB, CNRS UMR 5220, 69621 Villeurbanne Cedex, France (e-mail: arnaud.gelas@creatis.insa-lyon.fr; olivier.bernard@creatis.insa-lyon.fr; denis.friboulet@creatis.insa-lyon.fr; remy.prost@creatis.insa-lyon.fr).

Color versions of one or more of the figures in this paper are available online at <http://ieeexplore.ieee.org>.

Digital Object Identifier 10.1109/TIP.2007.898969

The level-set PDE is usually solved using now well-known finite differences schemes. These numerical schemes have been developed to obtain accurate and unique solutions, and involve upwind differencing, essentially nonoscillatory schemes borrowed from the numerical solutions of conservation laws and Hamilton Jacobi equations [4]. Most of the implementations of this scheme generally use two more specificities.

- *Narrow-banding*: In order to lower the computational cost, the solution is generally not computed on the whole image domain, but in a narrow band around the interface.
- *Reshaping* of the level set: In the course of propagation, the level-set function may develop steep or flat gradients, which, in turn, yield inaccuracies in the numerical approximation. This is usually taken into account by reshaping the level set through periodical re-initialization of the level-set function as the distance function to the interface.

In this paper, we describe an alternative technique to the usual finite difference framework, which consists of solving the level-set PDE through a collocation method using *radial basis functions* (RBFs).

Collocation can be seen as a particular case of the residual method for the computation of a numerical solution of a PDE. It consists of approximating the solution by a continuous function, which is, in turn, built as a linear combination of basis functions. The solution i.e., the parameters of the linear expansion, is obtained by prescribing the PDE to be verified on a particular set of points, usually called collocation points. In that sense, collocation may, thus, be seen as interpolating the PDE between the collocation points.

The use of RBFs as basis functions for collocation solution to PDE has been introduced in 1990 by Kansa in the field of computational fluid dynamics [5], [6]. RBFs have initially been introduced for solving multivariate scattered data interpolation problems because they provide such interpolation without requiring any underlying mesh. The interested reader will find in [7]–[9] a thorough review about applications and RBF fundamental properties. In the framework of collocation, the RBF meshless property translates into the fact that it yields a very flexible choice for the location of the collocation points.

Kansa's seminal paper has started a wealth of applications of RBF collocation in various fields such as astrophysics [10], heat transfer modeling [11], surface wind field computation [12], hydraulics [13], option pricing [14], magnetic field modeling [15], structural topology optimization in mechanics [16], and optimal feedback control [17]. Convergence and stability properties of the method have been studied in [18] and [19].

In the framework of our level-set application, the potential interests of using the RBF collocation strategy are the following.

- In contrast to the conventional finite difference narrow band implementations, the RBF collocation scheme allows an overall control of the level set (i.e., over the whole computational domain of the level set) with a reasonable computational cost.
- This computational cost may be further reduced through adapted algorithms, by using a particular class of RBFs, i.e., compactly supported RBFs (CSRBFs).
- Since the RBF representation¹ of the level set is parametric, it is relatively easy to constraint the propagation via constraints on the parameters. As it will be shown in the sequel, such constraints may be used to avoid the usual reinitialization step of the level set. As a consequence, the solution is topologically more flexible, since it may develop new contours (i.e., new zero level components), which are difficult to obtain when the narrow-band/reinitialization strategy is used.
- The smoothness of the solution is implicitly enforced, through the intrinsic smoothness of the underlying RBF representation. The RBF collocation formulation, thus, does not need to include the usual curvature term in the propagation equation.
- The obtained solution is continuous, the degree of continuity being imposed by the type of RBF chosen for the application. This is of interest for applications requiring the measure of differential properties of the interface, since quantities such as normals or curvatures may, thus, be accurately computed from this continuous representation.

The paper is structured as follows. In Section II, we recall the general form of the level-set propagation PDE and briefly review representation of shape through RBFs. In Section III, we give the expression of the numerical solution of the level-set PDE using RBF collocation and detail the implementation issues of the method. We discuss in particular the choice of CSRBF and show how the computational cost may be reduced using a kd -tree representation of neighborhoods. We also show how reinitialization of the level set may be avoided by constraining the l_1 -norm of the RBF parameters. We end this section by providing and discussing the overall complexity of the technique. In Section IV, we evaluate the behavior of the method using simulated images as well as medical images of various kinds, such as CT and US images. The main conclusions and perspective of this work are given in Section V.

II. THEORETICAL BACKGROUND

A. Usual Formulation

The level-set-based segmentation consists of capturing the shape to be recovered by propagating an interface which evolves according to the solution of a PDE derived from an energy functional. This energy criterion is designed in such a way that its minimum corresponds to the solution of the given problem. The energy functional is then minimized using variational calculus

¹In the case of strictly positive definite RBFs (see Section II-B).

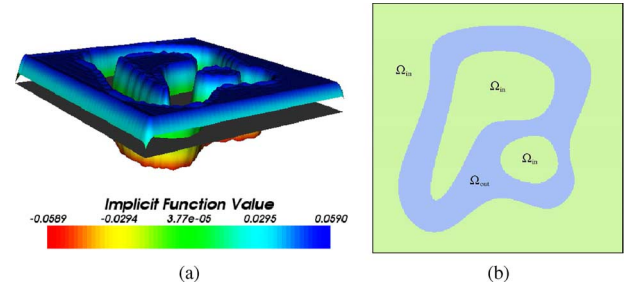


Fig. 1. Level-set function for a 2-D domain Ω represented as an elevation map \mathcal{S} , i.e., $z = f(\mathbf{p})$ (a). Interface Γ corresponds to the zero set of the level-set function, i.e., the intersection of \mathcal{S} and the horizontal plane $z = 0$ (a). Corresponding regions Ω_{in} and Ω_{out} are represented in (b).

techniques [3] and gradient descent method to get a PDE governing the motion of the interface.

In the level-set formalism, the interface Γ in \mathbb{R}^d is represented as the zero level set of a Lipschitz continuous function f of dimension $d + 1$, satisfying

$$\begin{cases} f(\mathbf{p}, t) > 0, & \text{for } \mathbf{p} \in \Omega_{\text{in}}(t) & (1) \\ f(\mathbf{p}, t) < 0, & \text{for } \mathbf{p} \in \Omega_{\text{out}}(t) & (2) \\ f(\mathbf{p}, t) = 0, & \text{for } \mathbf{p} \in \partial\Omega_{\text{in}}(t) = \Gamma(t) & (3) \end{cases}$$

where, considering an open region Ω in \mathbb{R}^{d+1} , Ω_{in} is a region in Ω bounded by Γ . Ω_{out} is defined as $\Omega_{\text{out}} = \Omega \setminus \Omega_{\text{in}}$ (see Fig. 1).

For brevity's sake, in the following, we consider the classical problem of segmenting one object (possibly having several non-connected components) from the background². This problem is typically handled by the evolution of one level set whose steady state partitions the image into two regions delimiting the boundaries of the object to be segmented. In this framework, a general expression of the energy functional driving the level set can be formulated as [21]

$$J(f) = \int_{\Omega} h(\mathbf{p}, f) \cdot \delta(f) \|\nabla f\| d\mathbf{p} + \mu_1 \cdot \int_{\Omega} k(\mathbf{p}, f) \cdot u(f) d\mathbf{p} + \mu_2 \cdot \int_{\Omega} g(\mathbf{p}, f) \cdot (1 - u(f)) d\mathbf{p} \quad (4)$$

where the first term is an energy criterion attached to the interface Γ (often referred to as contour term). The second and third terms (often referred to as region terms) are energy criteria attached to the inside and outside regions delimited by the interface Γ , respectively. u and δ are the Heaviside and Dirac univariate functions, respectively. μ_1 and μ_2 are some positive hyper-parameters.

Using variational calculus [3], [20], [22], the minimization of (4) leads to the following general evolution equation:

$$\frac{\partial f(\mathbf{p}, t)}{\partial t} + V(\mathbf{p}, t) \cdot \delta_{\epsilon}(f(\mathbf{p}, t)) = 0 \quad (5)$$

where δ_{ϵ} is a regularized version of the Dirac function [22] given as

$$\delta_{\epsilon}(x) = \frac{1}{\pi\epsilon \cdot \left(1 + \left(\frac{x}{\epsilon}\right)^2\right)} \quad (6)$$

where ϵ is a real positive constant and V is a velocity function which is derived from the variational scheme.

Depending on the specific application, V can be a function of the position \mathbf{p} , of geometrical properties of the interface and of images properties reflecting the object to be segmented.

Some authors modified the evolution (5) by substituting δ_ϵ by $\|\nabla f\|$. This operation does not affect the steady state solution and removes stiffness near the zero level set [20]. Moreover, the equation becomes independent of the scaling of the level-set function used and the problem becomes morphological. For more details refer to [3] and [23]. The evolution equation is then

$$\frac{\partial f(\mathbf{p}, t)}{\partial t} + V(\mathbf{p}, t) \cdot \|\nabla f(\mathbf{p}, t)\| = 0. \quad (7)$$

For clarity's sake, we use (5) in the following. As mentioned in the introduction, these evolution equations are commonly implemented using finite difference methods. These numerical schemes have been developed to obtain accurate and unique solutions, and involve upwind differencing, essentially nonoscillatory schemes borrowed from the numerical solutions of conservation laws and Hamilton Jacobi equations.

In traditional level-set methods [4], [24], the level-set function can develop flat or steep regions leading to difficulties in both numerical approximation of the derivatives and speed of convergence. In order to overcome this difficulty, the following scheme is generally used:

- initialize the level set as the distance function (relative to the interface);
- reshape the level-set function periodically in order to resurrect this distance function property.

Indeed, Mulder *et al.* showed in [25] that initializing f to a distance function and keeping its corresponding properties during the evolution process leads to more accurate numerical solutions than initializing f to a Heaviside function.

The most straightforward way of implementing the re-initialization operation is to extract the interface $f = 0$ and then explicitly compute the distance function from it. However, this method is generally time consuming. To overcome this difficulty, a now widely accepted method has been proposed [26] in order to re-initialize the level-set function by solving the following PDE:

$$\frac{\partial f(\mathbf{p}, t)}{\partial t} = \text{sign}(f_0(\mathbf{p}, t))(1 - \|\nabla f(\mathbf{p}, t)\|) \quad (8)$$

where f_0 is the function to be re-initialized and $\text{sign}(\cdot)$ is the sign function. However, if f_0 is not smooth or much steeper on one side of the interface than the other [4], the zero level set of the resulting function f can be moved away from that of the original function. For this reason, Li *et al.* recently proposed in [27] to add a new energy term to the general criterion (4)

$$J_{\text{reg}}(f) = \int_{\Omega} \frac{1}{2} (\|\nabla f(\mathbf{p}, t)\| - 1)^2 d\mathbf{p}. \quad (9)$$

This expression corresponds to a regularization term that penalizes the deviation of the level-set function from a signed distance function. This method has the main advantage to keep the

level-set function as a signed distance function without the need of the re-initialization.

B. Radial Basis Functions

RBFs² have become a popular approach for solving multivariate scattered data interpolation or approximation problems and is currently an active field of research. We give hereunder the outline of this approach and we refer the interested reader to [7] and [8] for more details.

Considering data $\{\mathbf{s}_i\}_{i=0, \dots, N-1}$ and their corresponding location $\{\mathbf{p}_i\}_{i=0, \dots, N-1}$ with $\mathbf{p}_i \in \Omega \subseteq \mathbb{R}^d$ and $\mathbf{s}_i \in \mathbb{R}$, the *interpolation* problems consist of finding a (continuous) function f such that $f(\mathbf{p}_i) = \mathbf{s}_i$ for $i = 0, \dots, N - 1$. If data locations, i.e., $\{\mathbf{p}_i\}$, do not lie on a uniform or regular grid, this problem is called *scattered data interpolation*. Unfortunately, this problem is clearly ill posed, i.e., there is an infinity of functions which can satisfy the respective conditions.

In the *scattered data interpolation* problem, a well-posed formulation can be achieved by using (*conditionally*) *positive definite kernels* [7]–[9]. If we make the assumption that there is no privileged direction, i.e., invariance under any orthogonal transformations (Euclidean rigid-body transformations), this naturally leads to RBFs.

The two main RBF types are *strictly positive definite* RBFs (SPD-RBFs) and *conditionally positive definite* RBFs (CPD-RBFs). Depending on the RBF type, the resulting function f and its coefficients have different expressions.

If SPD-RBFs [8, chapter 6] are used, f can be expressed as follows:

$$f(\mathbf{p}) = \sum_{i=0}^{N-1} \alpha_i \cdot \phi(\|\mathbf{p} - \mathbf{p}_i\|) \quad (10)$$

where ϕ is a RBF, $\{\mathbf{p}_i\}_{i=0, \dots, N-1}$ are called *centers*, and $\alpha = \{\alpha_i\}_{i=0, \dots, N-1}$ are called *coefficients*.

As shown in [8, chapter 6], SPD-RBFs may have a global support (i.e., $\phi(r) \neq 0, \forall r \in \mathbb{R}^+$) or a compact one (i.e., $\phi(r) = 0$ for r greater than σ). We will address this aspect in more details in Section III-A.

Coefficients are computed by solving

$$A \cdot \alpha = \mathbf{s} \quad (11)$$

where A is a square matrix of size N with

$$A_{ij} = \phi(\|\mathbf{p}_i - \mathbf{p}_j\|) \quad (12)$$

and \mathbf{s} is a column vector of size N whose elements are $\{\mathbf{s}_i\}$.

Since these RBFs are strictly positive definite, A is also strictly positive definite and is, thus, invertible.

In the case of CPD-RBFs [8, chapter 8], f can be expressed as follows:

$$f(\mathbf{p}) = \sum_{i=0}^{N-1} \alpha_i \cdot \phi(\|\mathbf{p} - \mathbf{p}_i\|) + \sum_{k=0}^{Q-1} \pi_k \cdot g_k(\mathbf{p}) \quad (13)$$

²The interested reader will find in [3] and [20] approaches which extend this method to several regions

where $\{g_k\}_{k=0,\dots,Q-1}$ is a basis in the m -dimensional null space containing all real-valued polynomials in d variables and of order at most m , $Q = \binom{m-1+d}{d}$, and we require $N \geq Q$, $\boldsymbol{\pi} = \{\pi_k\}_{k=0,\dots,Q-1}$ are called polynomial coefficients.

RBF coefficients $\{\boldsymbol{\alpha}\}$ and polynomial coefficients $\{\boldsymbol{\pi}\}$ are obtained by solving the following linear system:

$$\begin{bmatrix} A & G^T \\ G & 0 \end{bmatrix} \cdot \begin{bmatrix} \boldsymbol{\alpha} \\ \boldsymbol{\pi} \end{bmatrix} = \begin{bmatrix} \mathbf{s} \\ \mathbf{0} \end{bmatrix} \quad (14)$$

where $A_{ij} = \phi(\|\mathbf{p}_i - \mathbf{p}_j\|)$ and $G_{ki} = g_k(\mathbf{p}_i)$, and the second matrixial equation $G \cdot \boldsymbol{\alpha} = \mathbf{0}$ is an additive constraint which ensures the invertibility of the matrix.

From (10) and (13), a unified representation for the function f may be obtained for SPD- or CPD-RBFs. The evaluation of f for any point \mathbf{p} is expressed as the product of the one-line vector $\Phi(\mathbf{p})$ and a column vector $\boldsymbol{\mu}$

$$f(\mathbf{p}) = \Phi(\mathbf{p}) \cdot \boldsymbol{\mu} \quad (15)$$

and the associated system linking data \mathbf{s} and the expansion coefficients is noted as

$$H \cdot \boldsymbol{\mu} = \mathbf{q}. \quad (16)$$

In the *positive definite* case, we have

$$\Phi(\mathbf{p}) = [\phi(\|\mathbf{p} - \mathbf{p}_0\|), \dots, \phi(\|\mathbf{p} - \mathbf{p}_{N-1}\|)] \quad (17)$$

$$\boldsymbol{\mu} = \boldsymbol{\alpha} \quad (18)$$

$$H = A \quad (19)$$

$$\mathbf{q} = \mathbf{s}. \quad (20)$$

In the *conditionally positive definite* case, we have

$$\Phi(\mathbf{p}) = [\phi(\|\mathbf{p} - \mathbf{p}_0\|), \dots, \phi(\|\mathbf{p} - \mathbf{p}_{N-1}\|), g_0(\mathbf{p}), \dots, g_{Q-1}(\mathbf{p})] \quad (21)$$

$$\boldsymbol{\mu} = \begin{bmatrix} \boldsymbol{\alpha} \\ \boldsymbol{\pi} \end{bmatrix} \quad (22)$$

$$H = \begin{bmatrix} A & G^T \\ G & 0 \end{bmatrix} \quad (23)$$

$$\mathbf{q} = \begin{bmatrix} \mathbf{s} \\ \mathbf{0} \end{bmatrix}. \quad (24)$$

C. Implicit Interface

From an implicit function $f : \mathbb{R}^d \rightarrow \mathbb{R}$, we can define an *implicit contour*, *surface* or *hypersurface* depending on the dimension d , as the zero-set of the implicit function f . For convenience, we will say in the rest of this paper *implicit interface* for the zero-set of the implicit function f (see Fig. 2). An important property of implicit interface is the analytic computation of differential geometric quantities for a given point, such as normals $\mathbf{n}(\mathbf{p})$ (25), curvatures [Gauss–Kronecker curvature $K(\mathbf{p})$ (26) and mean curvature $H(\mathbf{p})$ for $d \geq 2$ (27)]

$$\mathbf{n}(\mathbf{p}) = -\frac{\nabla f(\mathbf{p})}{\|\nabla f(\mathbf{p})\|} \quad (25)$$

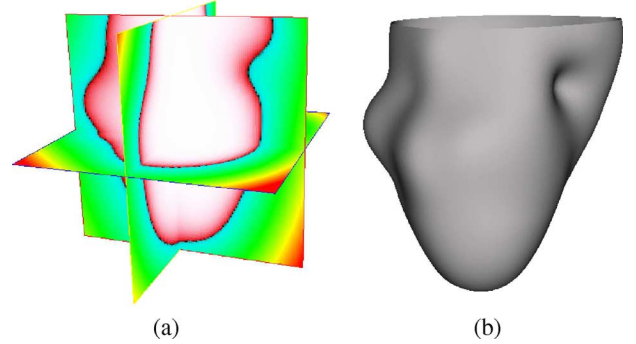


Fig. 2. Representation of the implicit function corresponding to (a) a human left ventricle and (b) its corresponding implicit interface.

$$K(\mathbf{p}) = \frac{(-1)^d}{\|\nabla f(\mathbf{p})\|^{d+1}} \nabla f(\mathbf{p})^T \cdot Hess_f(\mathbf{p}) \cdot \nabla f(\mathbf{p}) \quad (26)$$

$$H(\mathbf{p}) = \frac{1}{(d-1)\|\nabla f(\mathbf{p})\|} (\nabla f(\mathbf{p})^T Hess_f(\mathbf{p}) \cdot \nabla f(\mathbf{p}) - \|\nabla f(\mathbf{p})\|^2 \cdot tr(Hess_f(\mathbf{p}))) \quad (27)$$

with

$$\nabla f(\mathbf{p}) = \left[\frac{\partial f(\mathbf{p})}{\partial x_0}, \dots, \frac{\partial f(\mathbf{p})}{\partial x_d} \right]^T$$

and

$$Hess_f(\mathbf{p}) = \begin{bmatrix} \frac{\partial^2 f(\mathbf{p})}{\partial x_0^2} & \cdots & \frac{\partial^2 f(\mathbf{p})}{\partial x_0 \partial x_{d-1}} \\ \vdots & \ddots & \vdots \\ \frac{\partial^2 f(\mathbf{p})}{\partial x_{d-1} \partial x_0} & \cdots & \frac{\partial^2 f(\mathbf{p})}{\partial x_{d-1}^2} \end{bmatrix}.$$

III. SOLVING THE LEVEL-SETS EVOLUTION EQUATION USING RBF COLLOCATION

RBF collocation follows straightforwardly from the application of the RBF decomposition to the implicit function f (15), by assuming that space and time are separable i.e., the time dependence of f is only due to the coefficients $\boldsymbol{\mu}$. In such a case, this naturally leads to the following decomposition:

$$f(\mathbf{p}, t) = \Phi(\mathbf{p}) \cdot \boldsymbol{\mu}(t). \quad (28)$$

Substituting (28) into (5) yields the following ordinary differential equations (ODEs)

$$\Phi(\mathbf{p}) \cdot \frac{d\boldsymbol{\mu}(t)}{dt} + V(\mathbf{p}, t) \cdot \delta_\epsilon(\Phi(\mathbf{p}) \cdot \boldsymbol{\mu}(t)) = \mathbf{0}. \quad (29)$$

Equation (29) applies to every point \mathbf{p} of the domain Ω . In order to solve for the coefficients $\boldsymbol{\mu}$, these equations have to be sampled at N distinct locations, traditionally called *collocation points*. In the framework of RBF formulation, the collocation points are chosen to be the RBF centers, i.e., the \mathbf{p}_i , which is generally referred as *unsymmetric* collocation. This approach may, thus, be summarized through the following equation:

$$H \cdot \frac{d\boldsymbol{\mu}(t)}{dt} = -B(\boldsymbol{\mu}(t), t) \quad (30)$$

TABLE I
 WENDLAND'S RBF [28] FOR VARIOUS DIMENSION d AND CONTINUITY C^{2k} .
 THE SYMBOL \doteq DENOTES EQUALITY UP TO A MULTIPLICATIVE POSITIVE
 CONSTANT AND u IS THE HEAVISIDE FUNCTION. NOTE THAT WENDLAND'S
 RBF ARE THE SAME FOR $d = 2n$ AND $d = 2n + 1$

| Dimension d | $\phi(r)$ | Continuity |
|--------------------|---|------------|
| $d = 1$ | $\phi_{1,0}(r) = u(1 - r)$ | C^0 |
| | $\phi_{2,1}(r) \doteq u((1 - r)^3) (3r + 1)$ | C^2 |
| | $\phi_{3,2}(r) \doteq u((1 - r)^5) (38r^2 + 5r + 1)$ | C^4 |
| $d = 2$ or $d = 3$ | $\phi_{2,0}(r) = u((1 - r)^2)$ | C^0 |
| | $\phi_{3,1}(r) \doteq u((1 - r)^4) (4r + 1)$ | C^2 |
| | $\phi_{4,2}(r) \doteq u((1 - r)^6) (35r^2 + 18r + 3)$ | C^4 |

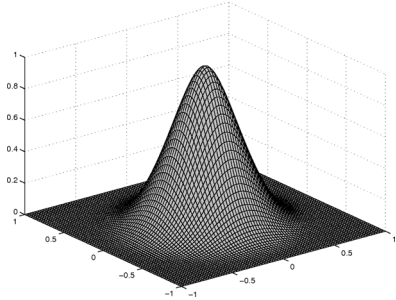


Fig. 3. Wendland's RBF with C^2 continuity and dimension $d = 2$.

where H is the interpolation matrix defined in Section II-B (16), and $B(\boldsymbol{\mu})$ is a column vector related to the level-set formalism used in (29), i.e.,

$$B(\boldsymbol{\mu}(t), t) = V(\mathbf{p}_i, t) \cdot \delta_\epsilon (\Phi(\mathbf{p}_i) \cdot \boldsymbol{\mu}(t)). \quad (31)$$

From (30), the level-set evolution is now cast into an ODE.

In the next section, we give implementation issues for solving this ODE with a low computational complexity and obtaining an efficient evolution of the level set.

A. Choice of Radial Basis Functions

1) *Compactly Supported RBFs*: From (30), the evolution of the level set will rely on the matrix H , and the evaluation of the vector $\Phi(\mathbf{p})$, which in turn depends on the choice of the underlying RBF (see Section II-B). In order to obtain a sparse interpolation matrix, and the possibility of a fast evaluation of the function f , authors have introduced recently compactly supported RBFs (CSRBFs) [8], [28]–[30]. While globally supported RBFs can be used for any dimension d , it is not exactly the same with compactly ones. Indeed, a compactly supported RBF is strictly positive definite on \mathbb{R}^d only for a fixed maximal d -value [8].

In [28], Wendland constructs a popular family $\phi_{d,k}$ of strictly positive definite CSRBFs, expressed with a polynomial form whose degree is minimal for a given dimension space d and whose continuity is C^{2k} . Whereas in [29], Wu presents another way to construct similar CSRBFs, but provides higher polynomial degree for a prescribed smoothness and dimension. In [8], Wendland gives a general formulation about the construction of strictly positive definite CSRBFs.

In this framework, we choose to build our implementation upon Wendland's CSRBFs (see Table I and Fig. 3 for one example of such RBF). It is to be noted that since all CSRBFs are *definite positive*, the following framework holds for any other CSRBFs.

The use of CSRBFs imply the choice of the support size. Formally, the implicit function is, thus, given as

$$f(\mathbf{p}) = \sum_{i=0}^{N-1} \alpha_i \cdot \phi_\sigma(\|\mathbf{p} - \mathbf{p}_i\|) \quad (32)$$

where $\phi_\sigma(\cdot) = \phi(\cdot/\sigma)$, and σ is the support size.

The choice of the support size σ results from a tradeoff: if the support size is chosen too small, the function will not be continuous, whereas if the support size is chosen too large, the interpolation matrix becomes dense and we loose the interest of using CSRBFs. Our proposal for the support size is directly related to the so-called *fill distance* $h_{\mathcal{P},\Omega}$, through the expression

$$\sigma = \rho \cdot h_{\mathcal{P},\Omega} \quad (33)$$

where $\rho > 1$ and $h_{\mathcal{P},\Omega}$ is defined as follows:

$$h_{\mathcal{P},\Omega} = \max_{\mathbf{p} \in \Omega} \min_{\mathbf{p}_i \in \mathcal{P}} \|\mathbf{p} - \mathbf{p}_i\|. \quad (34)$$

The *fill distance* can be interpreted as the radius of the largest ball which is completely contained in Ω and which does not contain any data site \mathbf{p}_i .

2) *Data Structure*: Because CSRBFs have finite support, many procedures of our method can be sped up by using efficient data structure for *range query* searches. Due to this compactness, only few centers should be considered for evaluating the implicit function at a point \mathbf{p} , or for computing each term of the interpolation matrix H . In our setting, given a region of space \mathcal{R} , this amounts to determining the set of CSRBF centers \mathcal{P} contained in \mathcal{R} .

There has been a considerable amount of work on devising efficient data structures for range query search, such as [31] and [32]. In our implementation, we use the *kd-tree* data structure [33], which is based on a recursive subdivision of space into disjoint axis aligned boxes. The principle of the *kd-tree* may be briefly described as follows. The root node of the *kd-tree* is a box which contains all data points \mathcal{P} and the whole domain Ω . Consider an arbitrary node in the tree, with its associated box B and points X . As long as the number of points contained in this node is greater than a prescribed quantity, the *bucket size*, this node is split into two new nodes. There are several splitting method to determine the hyperplane which will split the box and the points into two. We use the standard method, i.e., the splitting dimension is the dimension of the maximum spread of point set X , and the splitting value is the median value of the coordinates of X along the splitting dimension.

Detailed procedure to build the *kd-tree* can be found in [8, Algorithm 4, p. 239]. By following this algorithm, *kd-tree* can be constructed in $O(dN \log N)$ time and requires $O(dN)$ space in memory. With such data structure, *range query search* can be computed in $O(\log N)$ [8, Algorithm 5, p. 240].

B. RBF Centers Distribution and Velocity Sampling

As mentioned in the introduction, the RBF-based methods do not require any underlying mesh, or grid, i.e., we can use any centers spatial distribution adapted to the targeted application. When no *a priori* information about the shape to be segmented is available, the RBF centers may, thus, be simply located on a

regular grid. Conversely, if some knowledge about this shape is at hand, an interesting perspective consists of incorporating this information through an adapted centers distribution. In most examples given in the next section, no *a priori* known shape is assumed and regular grids are, therefore, used for RBF centers, while the interest of using an adapted, nonregular, center placement is illustrated on a particular case.

Once the centers have been placed, the collocation approach implies the evaluation of the application dependent velocity term $V(\mathbf{p}_i)$ in (31) at each RBF center \mathbf{p}_i . This is straightforward if the velocity is defined for any point in the computational domain Ω , as it is the case when the velocity term relies on region-based features [22], [34]. This may be an issue when the targeted segmentation application yields velocity terms that are defined only on the interface, i.e., depend on boundary-based features. As for conventional level-set implementation, this issue may nevertheless be easily addressed using the velocity extension methods developed for conventional level-set implementation [3].

Conventional RBF collocation methods [5], [6], [9] use pointwise sampling of $V(\mathbf{p}_i)$ at RBF centers, which is suitable when the underlying data are given with a very good accuracy as in the case of theoretical PDE resolution [5], [6]. Experimental images may however be corrupted by noise, making this pointwise sampling inappropriate, since the evolution of the interface would, thus, be driven by unreliable velocity terms. In such a case, the velocity is computed as the weighted average of the neighboring velocities.

C. Resolution of the ODEs

The resolution of the ODEs obtained through collocation requires the definition of an initial implicit function f^0 , i.e., the initial RBF expansion coefficients α_0 . In practice, the initialization may be provided as an interface, available either from *a priori* knowledge about the object to be segmented or from user interaction. In such a case, f^0 may be easily built as an implicit function whose zero level interpolates or approximates the given interface [35]–[37]. In the case where the initialization is given itself as an implicit function (see [38] and [39]), (11) may be directly applied to obtain f^0 .

Many numerical schemes may be then applied to solve the ODEs in (30), Euler's and Runge-Kutta being the most traditional. Our current implementation uses a simple first order forward Euler's method. As shown in the results section, this scheme yields accurate segmentation results and provides a fast evolution of the interface. Applying Euler's method to (30) yields

$$\alpha^{n+1} = \alpha^n - \tau \cdot H^{-1} \cdot B^n(\alpha^n) \quad (35)$$

where τ is the step size.

A straightforward approach for implementing the evolution (35) would consist of computing H^{-1} as an initial stage and then performing the propagation by computing the product $H^{-1} \cdot B^n(\alpha^n)$ at each iteration. This approach is inefficient since H^{-1} is not sparse and, thus, requires an important space in memory.

Fortunately, Wendland's CSRBFs are positive definite functions, and, as a consequence, the associated matrix H is also positive definite. Since H is moreover symmetric, we may use a LDLT or a Cholesky decomposition. In the current implementation, we use a sparse Cholesky decomposition from MUMPS library [40], i.e., $H = L \cdot L^T$ where L is a lower triangular matrix. The Cholesky decomposition (i.e., the matrix L) is computed as an initial stage, and for each iteration we solve the following triangular systems:

$$L \cdot \mathbf{u}^n = B^n(\alpha^n) \quad (36)$$

$$L^T \cdot \mathbf{v}^n = \mathbf{u}^n. \quad (37)$$

The RBF coefficients are finally given as

$$\alpha^{n+1} = \alpha^n - \tau \cdot \mathbf{v}^n. \quad (38)$$

D. Bounded Implicit Function

As mentioned in Section II-A, periodically reshaping the level as the interface signed distance function is a common strategy used for avoiding developing of steep regions in the implicit function near the zero level. This scheme increases the computational cost and reduces the topological flexibility of the method since it prevents the level set from creating new zero level components far away from the initial interface.

A similar problem appears in our collocation method: the implicit interface reaches a stable solution, however RBF coefficients can go on increasing. This may be shown as follows.

Proposition 1: In (35) $\|\alpha\|_1$ can increase slowly at each step, depending on τ .

Proof: By computing $\|\alpha^{n+1}\|_1$, it follows:

$$\|\alpha^{n+1}\|_1 \leq \|\alpha^n\|_1 + \tau \cdot \|H^{-1}\| \cdot \|B^n(\alpha^n)\|_1. \quad (39)$$

The higher bound of the l_1 -norm of (31) is

$$\|B^n(\alpha^n)\|_1 \leq \max_{\mathbf{p}_i \in \mathcal{P}} V(\mathbf{p}_i) \cdot \max_{x \in \mathbb{R}} \delta_\epsilon(x) \quad (40)$$

from (6) $\max_{x \in \mathbb{R}} \delta_\epsilon(x) = 1/\pi\epsilon$.

Thus, it follows that:

$$\|\alpha^{n+1}\| \leq \|\alpha^n\| + \gamma \quad (41)$$

where $\gamma = (\tau/(\pi \cdot \epsilon)) \cdot \|H^{-1}\| \cdot \max_{\mathbf{p}_i \in \mathcal{P}} V(\mathbf{p}_i) > 0$. By choosing a low τ value, at least a slow increasing of $\|\alpha^n\|_1$ can be obtained. ■

We propose here to take advantage of the linearity of the RBF expansion (10) in order to avoid the steep gradient problem and to preserve the topological flexibility at a low computational cost. In order to bound the implicit function f (hence, the norm of gradient $\|\nabla f\|$), while preserving the global shape of the implicit function and the implicit interface, we bound the expansion coefficients. Note that bounding the norm of the gradient results in constraining the Lipschitz constant.

As a starting point, we note that the multiplication of an implicit function f by a non-null coefficient k does not change its

TABLE II
COMPLEXITY OF THE VARIOUS COMPUTATION STAGES FOR GLOBALLY AND COMPACTLY SUPPORTED RBFs. NOTE THAT THE MULTIPOLE METHOD CAN BE APPLIED ONLY TO SOME GLOBAL RBFs [8] AND REQUIRES A COMPLEX ALGORITHMIC SETUP

| | Global Supported RBFs (using multipole method) | CSRBFs (using kd -tree data structure) |
|------------------------------|---|---|
| Computation to build H | $O(N^2)$ | $O(N \log N)$ |
| Computation to solve | $O(N \log N)$ | $O(nzf)$ |
| Computation to evaluate (15) | $O(\log N)$ | $O(\log N)$ |
| Effect of a single center | global | local |

associated interface.³ Since f is represented through the coefficients α of a RBF expansion, $k \cdot f$ simply corresponds to $k \cdot \alpha$.

For SPD-RBFs, especially Wendland's ones (see Table I), this provides us an easy way to bound the values of the implicit function. Indeed, due to the linearity of the SPD-RBF expansion, we may link this constraint to the l_1 -norm of α . Formally we have:

$$|f(\mathbf{p})| = \left| \sum_{i=0}^{N-1} \alpha_i \cdot \phi(\|\mathbf{p} - \mathbf{p}_i\|) \right| \leq \sum_{i=0}^{N-1} |\alpha_i| \cdot |\phi(\|\mathbf{p} - \mathbf{p}_i\|)| \leq K \cdot \|\alpha\|_1 \quad (42)$$

$$\|\nabla f(\mathbf{p})\|_2 = \left\| \sum_{i=0}^{N-1} \alpha_i \cdot \nabla \phi(\|\mathbf{p} - \mathbf{p}_i\|) \right\|_2 \leq \sum_{i=0}^{N-1} |\alpha_i| \cdot \|\nabla \phi(\|\mathbf{p} - \mathbf{p}_i\|)\|_2 \leq K' \cdot \|\alpha\|_1 \quad (43)$$

where $K = \max_{r \in [0, \infty[} |\phi(r)| = \phi(0)$, and $K' = \max_{r \in [0, \infty[} |\phi'(r)|$.

In our implementation, for $d = 2, 3$ we use C^2 Wendland's function (see Table I and Fig. 3), where K and K' are equal to 1 and 135/64, respectively.

In order to bound the implicit function (hence, its gradient norm), we apply a normalization on RBF coefficients which bounds $\|\alpha^n\|_1$ if $\|\alpha^n\|_1 > \beta$, where β is a positive constant.

The evolution equation becomes

$$\begin{cases} L \cdot \mathbf{u}^n = B^n(\tilde{\alpha}^n) & (44) \\ L^T \cdot \mathbf{v}^n = \mathbf{u}^n & (45) \\ \alpha^{n+1} = \tilde{\alpha}^n - \tau \cdot \mathbf{v}^n & (46) \\ \tilde{\alpha}^{n+1} = \frac{\beta}{\|\alpha^{n+1}\|_1} \cdot \alpha^{n+1}, & \text{if } \|\alpha^{n+1}\|_1 > \beta \\ \tilde{\alpha}^{n+1} = \alpha^{n+1}, & \text{else.} \end{cases} \quad (47)$$

In our implementation, β is set to σ , so the values of f are in the interval $[-\sigma, +\sigma]$. It is important to notice that the computational cost of this normalization is in $O(N)$.

E. Complexity

We provide in this section the complexity of the various computation stages of the proposed approach. In order to have a reference, it is compared to the complexity corresponding to the use of globally supported RBFs.

³We avoid $k = 0$ since the zero set of f would be the whole domain Ω .

The figures related to globally supported RBFs are provided by Morse [35] and Wendland [8] and rely on the following features.

- The matrix H is dense and its computation⁴ is $O(N^2)$.
- Using the multipole method implementation [8], solving the system is $O(N \log N)$ and the evaluation of the implicit function is $O(\log N)$.

In the case of the proposed CSRBFs, the following applies.

- Using a kd -tree data structure for the center set (see Section III-A2), the matrix H computation is $O(N \log N)$ and the implicit function f evaluation is $O(\log N)$.
- The computational complexity of sparse Cholesky factorization cannot be given in general since it depends on how sparse is H . However, according to [41], the factorization can be considered to be in $O(nzf)$, where nzf is the number of nonzero factors, which depends on the CSRBF centers distribution and on the CSRBF support size σ . In practice, we choose sufficiently small support, so nzf will be much smaller than N^3 .

The complexity of these implementations is given in Table II. It is to be noted that the multipole method can be applied only to some global RBFs [8] and requires a complex algorithmic setup, whereas the kd -tree data structure used for CSRBFs is quite general and straightforward to implement.

As noted by Osher [42], [43], the complexity of the usual narrow band method including reinitialization is $O(M \log M)$ where M is the total number of grid points in the narrow band. A more detailed comparison of the complexity of our method is not straightforward due to the following.

- It is difficult to relate the number of RBF centers N and the number of points in the narrow band M .
- The narrow band implementation provides a local control whereas our method provides a global control over the level set. This will yield different segmentation results in most cases.

IV. RESULTS

In this section we evaluate the proposed approach using simulated and medical images. In all experiments we use the general evolution equation given in (5) and consequently apply the RBF collocation framework given in (29), (31) and (44)–(47).

Such an approach implies the choice of the support ϵ of the regularized Dirac measure $\delta_\epsilon(x)$ defined in (6). As noted by Chan and Vese [22], this parameter has indeed to be large

⁴Due to the symmetry of H , complexity can be decreased in half; however, it is still in $O(N^2)$.

TABLE III
TIME IN SECONDS FOR PROCESSING VARIOUS IMAGES

| Experimental conditions | | | | Initialization | | Evolution of the interface to convergence | | |
|-------------------------|-----------------|----------------|----------|-----------------|------------------------|---|-----------------------|---------|
| Name | Image Size | Number of RBFs | β | Building of H | Cholesky decomposition | Computation of α^{n+1} (Euler steps) | Parameters estimation | Total |
| Simulation 1 | 311^2 | 100^2 | σ | 0.36 | 0.27 | 4.15 | 12.90 | 17.05 |
| Simulation 2 | 446^2 | 150^2 | σ | 0.84 | 1.03 | 10.68 | 19.48 | 28.29 |
| U.S. | 249×40 | 60×10 | σ | 0.47 | 0.03 | 3.56 | 14.28 | 17.34 |
| Calcaneous | 100^3 | 37^3 | σ | 37.23 | 223.82 | 852.34 | 1906.32 | 2758.66 |

enough so the evolution equation acts on all level curves and yields a global minimizer. Since f is bounded in the interval $[-\sigma, +\sigma]$ from (44), we, thus, simply set ϵ to 2σ in all experiments.

The use of CSRBF collocation implies a choice of the RBF support size σ . As mentioned in Section III-A.I, this parameter is related to the *fill distance* $h_{\mathcal{P},\Omega}$ as $\sigma = \rho \cdot h_{\mathcal{P},\Omega}$. Unless otherwise mentioned, we set $\rho = 4$ in our experiments, in order to ensure continuity of the reconstructed implicit function. A larger support would provide a smoother implicit function at the cost of a higher computational cost.

In (35), we use a forward Euler approach for time discretization, which implies the choice of the time step τ . Experimentally, we observe that for τ varying in the range $[0.1, 10]$, the segmentation remains unchanged. This result shows the robustness of the proposed method in the choice of the time step. Thus, we arbitrarily fix τ to 1 for each experiment.

Finally, in Table III, for each experiment we provide the *cpu* time corresponding to each step of the proposed algorithm. Calculations were performed on a 3.6-GHz Pentium IV with 2 Gigabytes of RAM.

A. Numerical Simulations

The segmentation examples given in this part are based on the Chan–Vese functional [22], which aims at partitioning the image into regions with piecewise constant intensity. This approach corresponds to a particular case of the Mumford–Shah functional [44], known as the minimal partition problem. This functional is given as

$$\begin{aligned}
 J_{\text{Mum}}(C_1(f), C_2(f), f) & \\
 &= \lambda_1 \cdot \int_{\Omega} \delta(f) \|\nabla f\| d\mathbf{p} + \lambda_2 \cdot \int_{\Omega} (I(\mathbf{p}) - C_1(f))^2 \cdot u(f) d\mathbf{p} \\
 &+ \lambda_3 \cdot \int_{\Omega} (I(\mathbf{p}) - C_2(f))^2 \cdot (1 - u(f)) d\mathbf{p} \quad (48)
 \end{aligned}$$

where λ_1 , λ_2 , and λ_3 are hyperparameters, $C_1(f)$ and $C_2(f)$ are constant calculated below, and I is the image to be segmented. $C_1(f)$ and $C_2(f)$ are computed at each iteration using the following expressions:

$$\left\{ \begin{aligned} C_1(f) &= \frac{\int_{\Omega} I(\mathbf{p}) \cdot u(f(\mathbf{p}, t)) d\mathbf{p}}{\int_{\Omega} u(f(\mathbf{p}, t)) d\mathbf{p}} \quad (49) \\ C_2(f) &= \frac{\int_{\Omega} I(\mathbf{p}) \cdot (1 - u(f(\mathbf{p}, t))) d\mathbf{p}}{\int_{\Omega} (1 - u(f(\mathbf{p}, t))) d\mathbf{p}}. \quad (50) \end{aligned} \right.$$

Due to the intrinsic smoothness of the RBF formulation, the smoothness term of the functional is not used (we set $\lambda_1 = 0$). The two remaining hyperparameters (λ_2 and λ_3) are set to 1.

In this framework, the velocity term used in our examples is then given as

$$V(\mathbf{p}, t) = -(I(\mathbf{p}) - C_1(f))^2 + (I(\mathbf{p}) - C_2(f))^2. \quad (51)$$

1) *Simulation 1*: Fig. 4 illustrates the application of the method to an image containing a shape with two holes and blurred contours. The method has been applied for various additive noise levels, as shown on Fig. 4(a)–(c). For this simulation, no *a priori* knowledge about the shape to segment is considered and the RBF centers are, thus, positioned on a regular rectangular grid with 100×100 nodes.

Fig. 4(d) shows the segmentation obtained from the noise-free image. Our approach detects the shape and automatically handles the required topology changes. Fig. 4(e) and (f) shows that in the presence of additional noise (corresponding to a SNR value of 30 and 20 dB, respectively) the model still provides a correct segmentation. However, we note that the detected interface is not as smooth as the original shape. As previously mentioned, the smoothness of the interface may be adjusted by selecting an appropriate support size σ . Fig. 5 shows the segmentations obtained with larger supports in the case of a 20 dB SNR.

The influence of the normalization procedure described in Section III-D is studied using the results corresponding Fig. 4(b). Fig. 6(a) shows the level set after 100 iterations when normalization is not applied and illustrates resulting steep gradient of the implicit function near the zero level. As previously mentioned, this could be avoided by the conventional reinitialization of the level set to a signed distance function. Fig. 6(b) presents the obtained level set when our normalization (47) is applied: the implicit function f is bounded in the range $[-\sigma, +\sigma]$.

The influence of the normalization may be investigated by studying the variation of the RBF coefficients versus the iteration step number. We measure here this variation by computing the l_{∞} -norm of the difference of the RBF coefficients between consecutive iterations. Without normalization Fig. 7(a) shows that the variation of the RBF coefficients reaches a constant nonzero value after 15 iterations, which corresponds to the convergence of the energy criterion J_{Mum} (48) [see Fig. 7(b)]. This illustrates the predicted phenomenon of the Section III-D: the implicit function keeps on evolving, even though the interface has reached the desired solution, i.e., convergence may be evaluated only locally. Fig. 7(c) gives the variation of the RBF coefficients when our normalization (47) is applied. In this case,

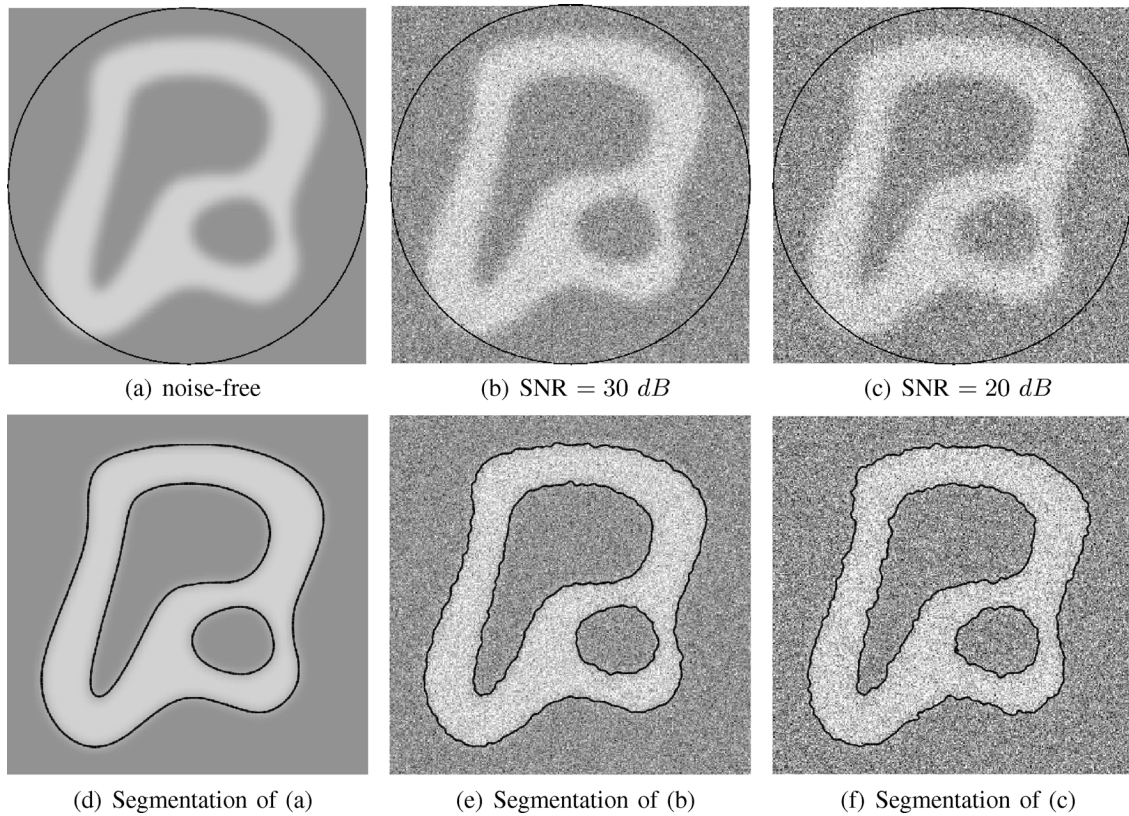


Fig. 4. Segmentation of an image containing a shape with two holes and blurred contours. The method is applied for various additive noise levels; 100×100 RBFs have been used in the experiment. Top row: Original images and initial interfaces. Bottom row: Corresponding segmentations.

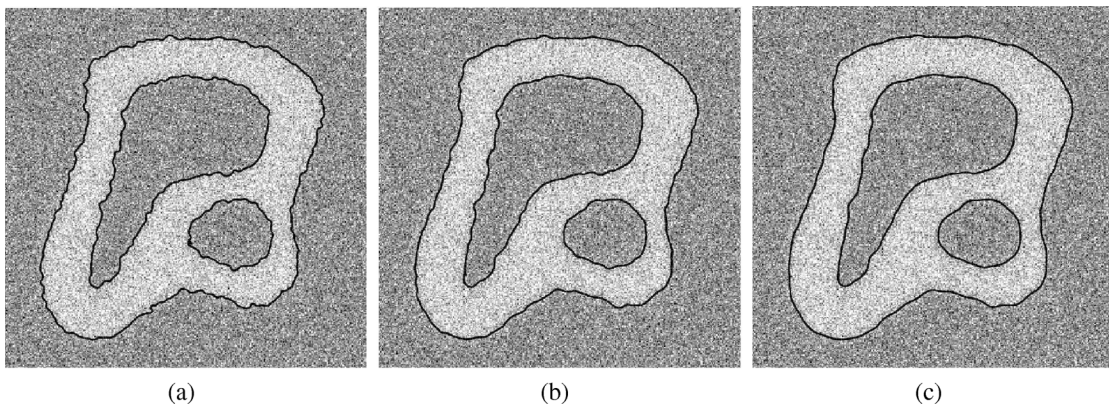


Fig. 5. Segmentation of the image with a 20-dB SNR given in Fig. 4(c) for increasing CSRBF support size. (a) $\sigma = 4 \cdot h_{\mathcal{P},\Omega}$; (b) $\sigma = 8 \cdot h_{\mathcal{P},\Omega}$; (c) $\sigma = 16 \cdot h_{\mathcal{P},\Omega}$.

the variation tends to stabilize to zero. This indicates that the level set globally converges to a stable solution. This observation suggests a simple way to check whether the implicit interface reached the solution, by looking at the variation of RBF coefficients. We give in Appendix I a heuristic argument supporting the behavior of the level set observed in Fig. 7(c).

2) *Simulation 2:* The second simulation addresses the influence of the number of CSRBF centers on the segmentation quality, using an image having high local curvature (see Fig. 8).

Segmentation is first performed using a regular rectangular grid applied on the whole domain with various numbers of centers (400, 1600, and 22 500). Fig. 8 shows how the accuracy of

the obtained segmentation increases with the number of centers involved.

As previously mentioned, the spatial distribution of the RBF centers may be arbitrary (i.e., they need not to lie on a regular grid) and this feature may be used to incorporate *a priori* knowledge on shape. This is illustrated in Fig. 9, where the RBF centers are distributed according to the shape to be recovered. In this simple example, the density of RBF centers is increased near the boundary to be detected. Fig. 9(a), (b), (d), and (e) shows the center location for 5 000 and 10 000 centers, respectively. As in the previous example, the segmentations presented in Fig. 9(c) and (f) shows that the number of centers directly influences the

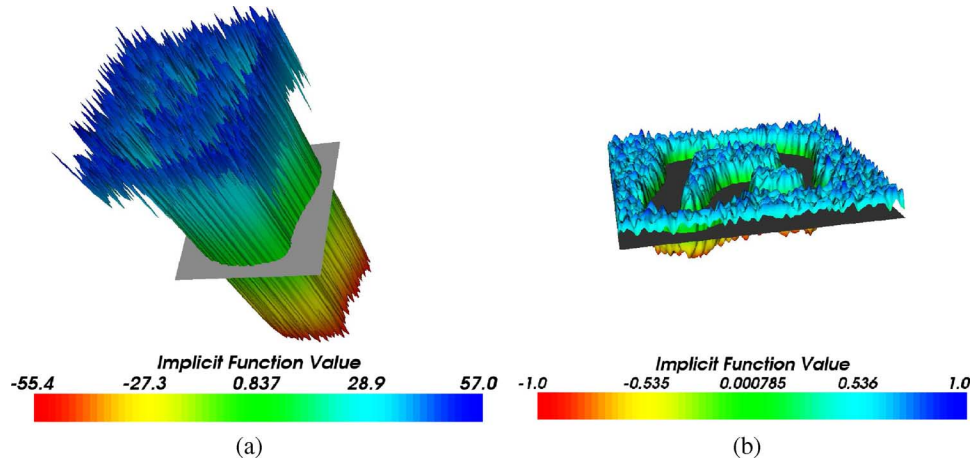


Fig. 6. Representation of the implicit function f after 100 iterations, (a) without normalization and (b) with normalization.

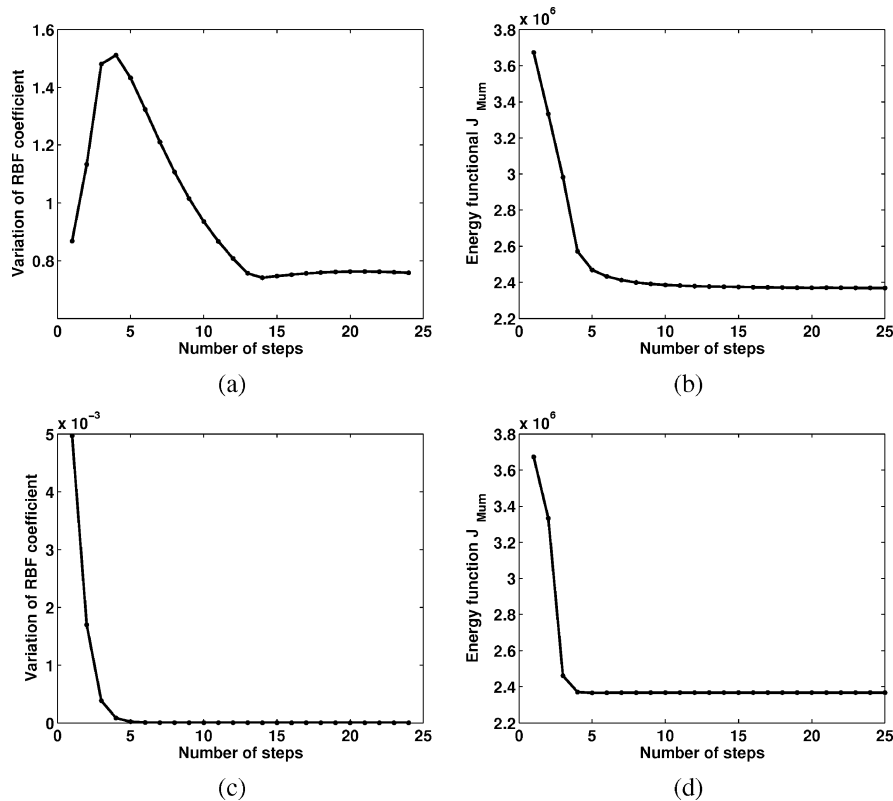


Fig. 7. Variation of RBF Coefficients versus the iteration step number (a) without normalization and (c) with normalization. Energy J_{Mum} versus the iteration step number (b) without normalization and (d) with normalization.

accuracy of the result. However, comparison of Figs. 8(c) and 9(f) indicates that the adapted centers distribution yields qualitatively the same accuracy using less centers. This example provides a very simple example of the interest of making the centers distribution adaptive. More sophisticated strategies could obviously be considered to improve centers placement, such as:

- Using *a priori* shape information: The centers distribution could be constrained through shape training (using ACP shape analysis, for instance [3], [45]);
- Using image features: The centers location and density should be linked image regions exhibiting salient shape features (i.e., gradient maxima, variation of regional statistical properties, etc., depending on the application).

B. Experimental Medical Data

1) *Calcaneus Bone in 3-D*: The proposed segmentation approach has been applied to 3-D CT images of calcaneus bone, with a $80 \mu\text{m}^3$ voxel size. Due to its complex topology, calcaneus bone is an attractive example for testing a level-set approach. As in the simulation section, Chan–Vese functional [22] and the associated velocity term (51) was used. Because of the complexity of the shape to be recovered, the RBF centers were distributed on a regular rectangular grid. Fig. 10 provides a 3-D visualization of the obtained segmentation as well as two corresponding image slices. These results show the ability of the model to handle complex topology.

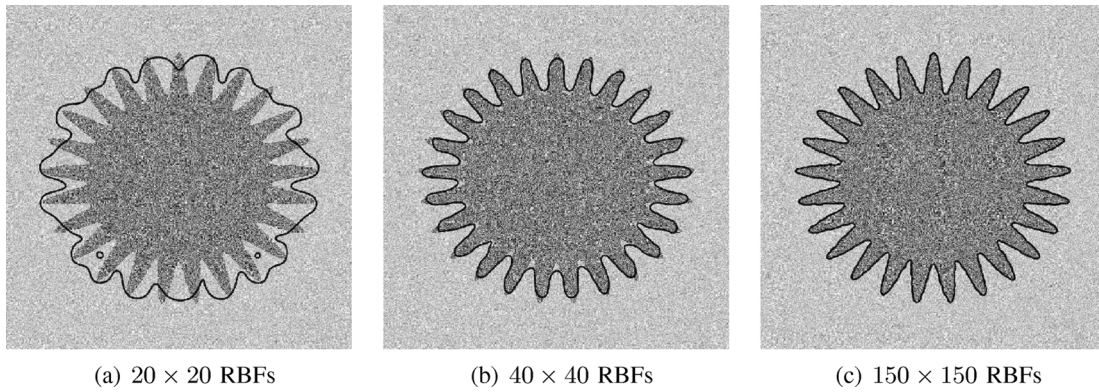


Fig. 8. Segmentation of a shape containing high curvatures for an increasing number of CSRBFs. The CSRBF centers are located on a regular rectangular grid.

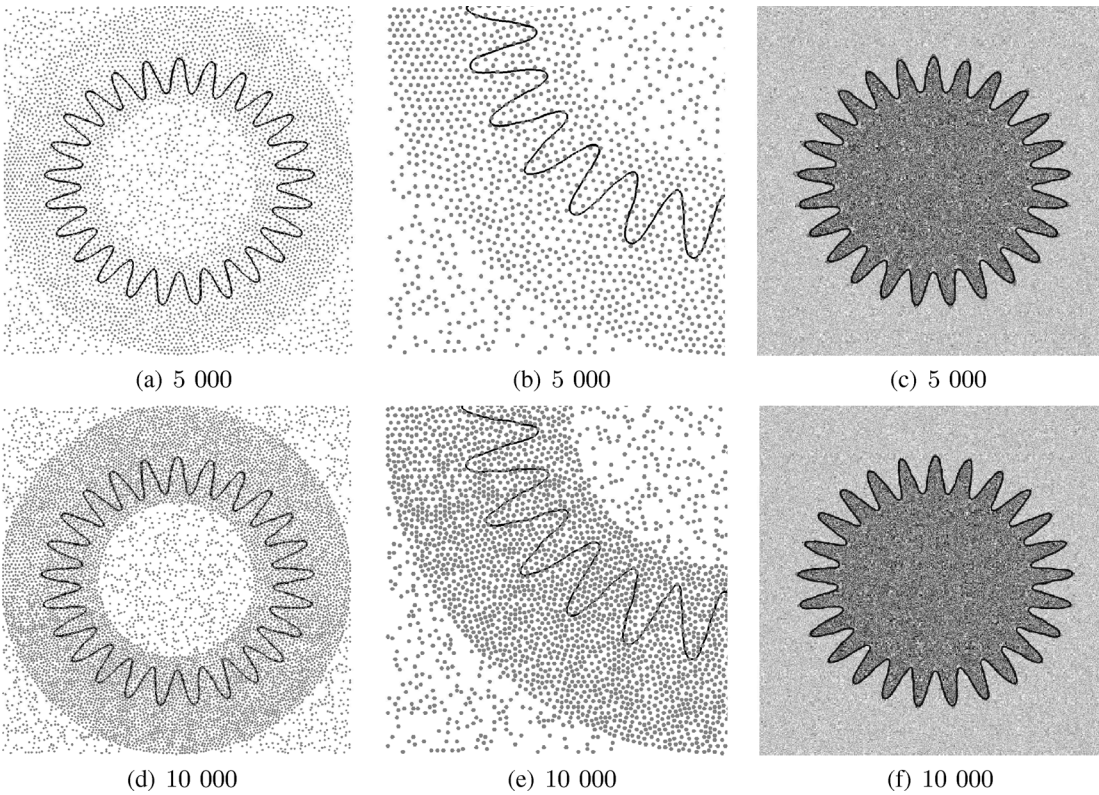


Fig. 9. Segmentation of a shape containing high curvatures using irregular CSRBF centers placement. Top row: Results for 5000 RBFs, centers distribution along with (a) the interface, (b) close-up of the centers distribution, and (c) resulting segmentation. Bottom row: Results for 10000 RBF centers distribution along with (d) the interface, (e) close-up of the centers distribution, and (f) resulting segmentation.

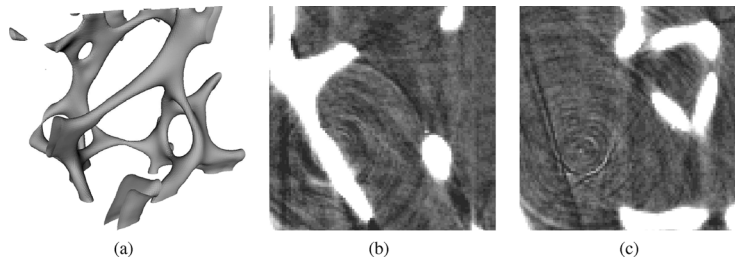


Fig. 10. Segmentation of 3-D CT images of calcaneus bone; 3-D rendering of the resulting segmentation. (a) Two slices through the original data volume (b) and (c).

An attractive feature of our approach lies in the fact that it provides a continuous representation of the implicit function embedding the interface. As mentioned in Section II-C, this feature provides analytical access to the differential properties of the interface, such as Gaussian and Mean curvatures. This is

illustrated in Fig. 11, which presents the distribution of these quantities over the surface of the segmented calcaneus bone.

2) *Ultrasound Images*: In this section, we apply our approach to echocardiographic ultrasound images. Segmentation of echocardiographic images is a difficult task, due to the speci-

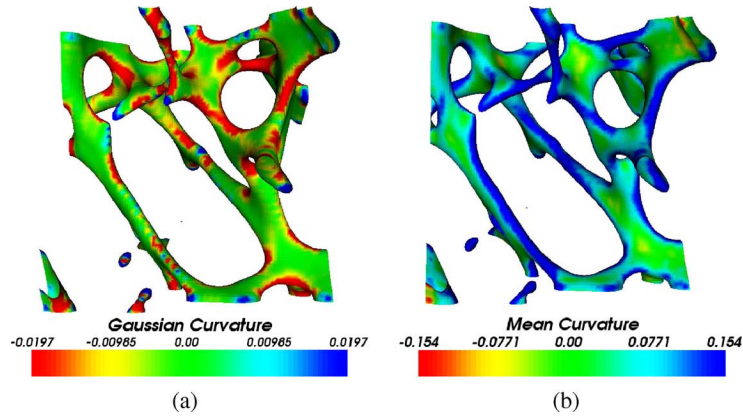


Fig. 11. Distribution of (a) the Gaussian and (b) mean curvature over the surface of the segmented calcaneus bone.

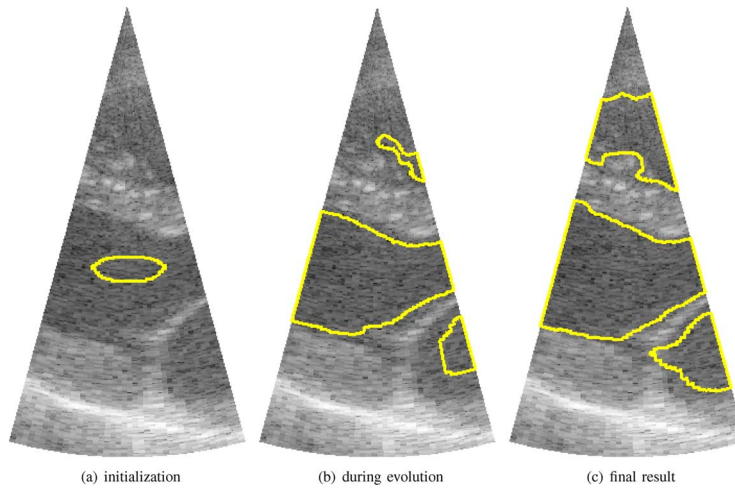


Fig. 12. Segmentation of echocardiographic data corresponding to a parasternal long axis view of the heart. Original image along with (a) the initial interface, (b) intermediate state of the interface during evolution of the level set, and (c) final segmentation.

ficiencies of the ultrasound acquisition which yields speckle and blurred boundaries related to diffuse scattering and attenuation.

In this context, we use the framework initially described by [34] which relies on evolving the interface in such a way that the resulting segmentation maximizes *a posteriori* probability of distribution of the image intensity in the inside and outside region. The velocity term may be derived by following the approach we described in [46], which shows that the statistics of the ultrasound signal corresponding to blood and myocardial regions may be described by generalized Gaussian distributions. The velocity term is then given as

$$V(\mathbf{p}, t) = -\log \left(\prod_{i=1}^m \left(\frac{P\left(\frac{I_i}{\xi_{in}, \vartheta_{in}}\right)}{P\left(\frac{I_i}{\xi_{out}, \vartheta_{out}}\right)} \right)^{1/m} \right) \quad (52)$$

where P corresponds to the Generalized Gaussian distribution, ξ and ϑ represent the shape and scaling parameters of the Generalized Gaussian distribution, respectively, computed inside and outside the moving interface at each iteration, m is the size of a circular window centered at \mathbf{p} and I_i is the intensity of the image at pixel location i .

For this test, the RBF centers are distributed on a regular rectangular grid with 600 nodes. Fig. 12 provides the segmentation obtained from a parasternal long axis view with a narrow angle focused on the inferolateral wall. This type of image is frequently used in clinical routine in order to accurately locate and track a region of the myocardium during the cardiac cycle. From an initialization located inside the left ventricle, our approach yields proper segmentation of all the blood/tissue interfaces in the image. This result shows the ability of the proposed approach to deal with noisy images using a statistical region-based segmentation.

C. Computation Times

We present in Table III the computation times associated to the above described experiments. Table III shows that the computation times associated to the Euler steps are reasonable, on the order of a few seconds for 2-D images and of a few minutes for the 3-D calcaneus image. The total time needed to obtain the segmentation is much larger. This time is, however, not linked to the proposed RBF collocation method, since it mainly results from the computation of the parameters associated to the velocity terms (i.e., $C_1(f)$ and $C_2(f)$ for the Chan–Vese method [22] and ξ and ϑ for the generalized Gaussian for the Zhu–Yuille

method [34]). This computation overhead would, thus, be the same for a conventional level-set implementation.

V. CONCLUSION

In this paper, we proposed a CSRBF collocation approach for segmentation using level sets. In contrast to the conventional finite difference with narrow band implementations, this numerical scheme yields an overall control of the level set over the computational domain and provides a parametric continuous solution. Due to this overall control and using CSRBF representation, the level set may be easily constrained. This feature avoids periodical reinitialization of the level set in the course of its propagation. In this way, the obtained segmentation is topologically more flexible, since it may develop new zero level components and is, thus, less dependent upon the initialization. As a further interest, we have shown that both the use of CSRBFs and *kd*-tree based representation of the RBF centers allows a significant reduction of the computational cost. The flexibility and performances of the proposed approach have been proved from simulations as well as medical image segmentations.

APPENDIX

CONVERGENCE OF THE NORMALIZED RBF COEFFICIENTS

A global convergence of the level set is obtained if the following proposition is satisfied:

$$\|\tilde{\alpha}^{n+1} - \tilde{\alpha}^n\|_1 \leq \|\tilde{\alpha}^n - \tilde{\alpha}^{n-1}\|_1. \quad (53)$$

To prove (53), we pursue the following steps.

Lemma 1:

$$\|\tilde{\alpha}^{n+1} - \tilde{\alpha}^n\|_1 \leq \|\alpha^{n+1} - \alpha^n\|_1. \quad (54)$$

Proof: The normalization operator used in (47) is a projection operator onto the convex set \mathcal{C} of l_1 -norm β -bounded vectors.

- Clearly, \mathcal{C} is a closed convex set, i.e.,

$$\mathbf{u}, \mathbf{v} \in \mathcal{C} \Rightarrow \mu \cdot \mathbf{u} + (1 - \mu) \cdot \mathbf{v} \in \mathcal{C} \text{ for } 0 \leq \mu \leq 1. \quad (55)$$

To prove (55), we consider $\mathbf{u}, \mathbf{v} \in \mathcal{C}$, then $\|\mathbf{u}\|_1 \leq \beta$, $\|\mathbf{v}\|_1 \leq \beta$. It follows $\|\mu \cdot \mathbf{u} + (1 - \mu) \cdot \mathbf{v}\|_1 \leq \mu\|\mathbf{u}\|_1 + (1 - \mu) \cdot \|\mathbf{v}\|_1 \leq \beta$.

It is easy to prove the closure by considering a given sequence $\{\mathbf{u}_n\} \subset \mathcal{C}$ such that $\lim_{n \rightarrow \infty} \|\mathbf{u}_n - \mathbf{u}\|_1 = 0$ implies $\mathbf{u} \in \mathcal{C}$.

- Now consider the operator

$$\begin{cases} P(\mathbf{w}) = \frac{\beta}{\|\mathbf{w}\|_1} \cdot \mathbf{w}, & \text{if } \|\mathbf{w}\|_1 > \beta \\ P(\mathbf{w}) = \mathbf{w}, & \text{else} \end{cases}. \quad (56)$$

This operator is a projection operator onto the closed set \mathcal{C} (POCS). In order to verify this conjecture, it is sufficient to show that for an arbitrary $\mathbf{w} \notin \mathcal{C}$ its projection onto \mathcal{C} is its closest point of \mathcal{C}

$$\|\mathbf{w} - P(\mathbf{w})\|_1 = \inf_{\mathbf{v} \in \mathcal{C}} \|\mathbf{w} - \mathbf{v}\|_1. \quad (57)$$

This condition can be easily verified as follows.

Clearly, $\|\mathbf{w} - \mathbf{v}\|_1$ is minimum if \mathbf{v} is collinear to \mathbf{w} , i.e., $\mathbf{v} = (\|\mathbf{v}\|_1/\|\mathbf{w}\|_1)\mathbf{w}$. Then

$$\inf_{\mathbf{v} \in \mathcal{C}} \|\mathbf{w} - \mathbf{v}\|_1 = \inf_{\mathbf{v} \in \mathcal{C}} \|\mathbf{w}\|_1 \cdot \left| 1 - \frac{\|\mathbf{v}\|_1}{\|\mathbf{w}\|_1} \right| = \|\mathbf{w}\|_1 \cdot \left| 1 - \frac{\beta}{\|\mathbf{w}\|_1} \right|. \quad (58)$$

According to (56), the left side of (57) can be rewritten as

$$\|\mathbf{w} - P(\mathbf{w})\|_1 = \|\mathbf{w}\|_1 \cdot \left| 1 - \frac{\beta}{\|\mathbf{w}\|_1} \right|. \quad (59)$$

That proves the equality of both sides of (57)

A POCS is a nonexpansive operator

$$\|P(\mathbf{w}_1) - P(\mathbf{w}_2)\|_1 \leq \|\mathbf{w}_1 - \mathbf{w}_2\|_1, \text{ for } \mathbf{w}_1, \mathbf{w}_2 \notin \mathcal{C}. \quad (60)$$

That proves the lemma 1. ■

We recall (47) $\alpha^{n+1} = \tilde{\alpha}^n - \tau H^{-1} B^n(\tilde{\alpha}^n)$.

By combining two consecutive equations, we can write

$$\begin{aligned} \|\alpha^{n+1} - \alpha^n\|_1 &= \|\tilde{\alpha}^n - \tilde{\alpha}^{n-1} - \tau H^{-1} \\ &\cdot [B^n(\tilde{\alpha}^n) - B^{n-1}(\tilde{\alpha}^{n-1})]\|_1. \end{aligned} \quad (61)$$

The terms $B^n(\tilde{\alpha}^n)$ and $B^{n-1}(\tilde{\alpha}^{n-1})$ are data dependent. According to (31), with the choice $\epsilon = 2\sigma = \beta$ (see Sections III-D and IV), the term $B^n(\tilde{\alpha}^n)$ weakly depends on $\tilde{\alpha}^n$

$$B^n(\tilde{\alpha}^n) \approx \frac{1}{\pi\epsilon} V^n \quad (62)$$

where V^n is the velocity function at iteration n .

Using the hypothesis of a consistent choice of the velocity, V^n becomes stationary in the vicinity of the region to be segmented and, consequently, $V^n - V^{n-1}$ vanishes.

Then, $\|\alpha^{n+1} - \alpha^n\|_1 = \|\tilde{\alpha}^n - \tilde{\alpha}^{n-1}\|_1$ and according to lemma 1, it demonstrates the convergence condition (53).

ACKNOWLEDGMENT

The authors would like to thank Dr. F. Peyrin from CREATIS at Lyon and ESRF (European Synchrotron Radiation Facility) at Grenoble, France, for data from Synchrotron X-Ray CT of calcaneus bone. They would also like to thank R. Haddad and Dr. P. Clarysse from CREATIS at Lyon for the data of the human left ventricle and J. Dhooge from Cardiac Ultrasound Research, University Hospital of Leuven (Belgium), for providing the cardiac ultrasound data.

REFERENCES

- [1] S. Osher and J. Sethian, "Fronts propagating with curvature-dependent speed: Algorithms based on Hamilton-Jacobi formulations," *J. Comput. Phys.*, vol. 79, no. 1, pp. 12–49, 1988.
- [2] J. Suri, K. Liu, S. Singh, S. Laxminarayan, X. Zeng, and L. Reden, "Shape recovery algorithms using level sets in 2-D/3-D medical imagery: A state-of-the-art review," *IEEE Trans. Inf. Technol. Biomed.*, vol. 6, no. 1, pp. 8–28, Jan. 2002.
- [3] R. Tsai and S. Osher, "Level set methods and their applications in image science," *Commun. Math. Sci.*, vol. 1, no. 4, pp. 1–20, 2003.
- [4] S. Osher and R. Fedkiw, *Level Set Methods and Dynamic Implicit Surfaces*. New York: Springer-Verlag, 2002.

- [5] E. J. Kansa, "Multiquadrics—A scattered data approximation scheme with applications to computational fluid-dynamics—I: Surface approximations and partial derivative estimates," *Comput. Math. Appl.*, vol. 19, pp. 127–145, 1990.
- [6] E. J. Kansa, "Multiquadrics—A scattered data approximation scheme with applications to computational fluid-dynamics—II: Solutions to parabolic, hyperbolic and elliptic partial differential equations," *Comput. Math. Appl.*, vol. 19, pp. 147–161, 1990.
- [7] M. D. Buhmann, *Radial Basis Functions: Theory and Implementations*, P. Ciarlet, A. Iserles, R. Kohn, and M. Wright, Eds. Cambridge, U.K.: Cambridge Univ. Press, 2003, vol. 12, Cambridge Monographs Appl. Comput. Math.
- [8] H. Wendland, *Scattered Data Approximation*, P. Ciarlet, A. Iserles, R. Kohn, and M. Wright, Eds. Cambridge, U.K.: Cambridge Univ. Press, 2005.
- [9] G. Fasshauer, "Meshfree methods," in *Handbook of Theoretical and Computational Nanotechnology*, M. Rieth and W. Schommers, Eds. Valencia, CA: American Scientific Publishers, 2006.
- [10] M. R. Dubal, "Construction of three-dimensional black-hole initial data via multiquadrics," *Phys. Rev. D*, vol. 45, no. 4, pp. 1178–1187, 1992.
- [11] M. Zerroukat, H. Power, and C. S. Chen, "A numerical method for heat transfer problems using collocation and radial basis functions," *Int. J. Numer. Meth. Eng.*, vol. 42, no. 7, pp. 1263–1278, 1998.
- [12] F. Hickernell and Y. C. Hon, "Radial basis function approximation of the surface wind field from scattered data," *Int. J. Appl. Sci. Comput.*, vol. 4, no. 3, pp. 221–247, 1998.
- [13] Y.-C. Hon, K. Cheung, X.-Z. Mao, and E. J. Kansa, "A multiquadric solution for the shallow water equations," *J. Hydraul. Eng.*, vol. 125, no. 5, pp. 524–533, 1999.
- [14] Y.-C. Hon and X.-Z. Mao, "A radial basis function method for solving options pricing models," *J. Finan. Eng.*, vol. 8, no. 1, pp. 31–50, 1999.
- [15] S. L. Ho, S. Yang, H. C. Wong, and G. Ni, "A meshless collocation method based on radial basis functions and wavelets," *IEEE Trans. Magn.*, vol. 40, no. 2, pp. 1021–1024, Mar. 2004.
- [16] S. Wang and M. Wang, "Radial basis functions and level set method for structural topology optimization," *Int. J. Numer. Meth. Eng.*, vol. 65, pp. 2060–2090, 2006.
- [17] C.-S. Huang, S. Wang, C. Chen, and Z.-C. Li, "A radial basis collocation method for Hamilton–Jacobi–Bellman equations," *Automatica*, 2006, to be published.
- [18] C. Franke and R. Schaback, "Solving partial differential equations by collocation using radial basis functions," *Appl. Math. Comput.*, vol. 93, no. 1, pp. 73–82, 1998.
- [19] J. Li, Y. Hon, and C. Chen, "Numerical comparisons of two meshless methods using radial basis functions," *Eng. Anal. Boundary Elem.*, vol. 26, no. 3, pp. 205–225, 2002.
- [20] H. Zhao, T. Chan, B. Merriman, and S. Osher, "A variational level set approach to multiphase motion," *J. Comput. Phys.*, vol. 127, pp. 179–195, 1996.
- [21] S. Jehan-Besson, M. Barlaud, and G. Aubert, "DREAM² S: Deformable regions driven by an Eulerian accurate minimization method for image and video segmentation," *Int. J. Comput. Vis.*, vol. 53, no. 1, pp. 45–70, 2003.
- [22] T. F. Chan and L. A. Vese, "Active contours without edges," *IEEE Trans. Image Process.*, vol. 10, no. 2, pp. 266–277, Feb. 2001.
- [23] L. Alvarez, F. Guichard, P. L. Lions, and J.-M. Morel, "Axioms and fundamental equations of image processing," *Arch. Ration. Mech. Anal.*, vol. 123, pp. 199–257, 1993.
- [24] V. Caselles, R. Kimmel, and G. Sapiro, "Geodesic active contours," *Int. J. Comput. Vis.*, vol. 22, 1997.
- [25] W. Mulder, S. Osher, and J. A. Sethian, "Computing interface motion in compressible gas dynamics," *J. Comput. Phys.*, vol. 100, pp. 209–228, Jun. 1992.
- [26] M. Sussman and E. Fatemi, "An efficient, interfacepreserving level set redistancing algorithm and its application to interfacial incompressible fluid flow," *SIAM J. Sci. Comput.*, vol. 20, pp. 1165–1191, 1999.
- [27] C. Li, C. Xu, C. Gui, and M. Fox, "Level set evolution without re-initialization: A new variational formulation," in *Proc. IEEE Int. Conf. Computer Vision and Pattern Recognition*, San Diego, CA, Jul. 2005, vol. 1, pp. 430–436.
- [28] H. Wendland, "Piecewise polynomial, positive definite and compactly supported radial basis functions of minimal degree," *Adv. Comput. Math.*, vol. 4, pp. 389–396, 1995.
- [29] Z. Wu, "Multivariate compactly supported positive definite radial functions," *Adv. Comput. Math.*, vol. 4, pp. 283–292, 1995.
- [30] M. D. Buhmann, "A new class of radial basis functions with compact support," *Math. Comput.*, vol. 70, no. 233, pp. 307–318, 2001.
- [31] K. L. Clarkson, "Nearest neighbor queries in metric spaces," in *Proc. 29th Annu. ACM Symp. Theory Comput.*, 1997, pp. 609–617.
- [32] F. P. Preparata and M. I. Shamos, *Computational Geometry*. Berlin, Germany: Springer-Verlag, 1985.
- [33] J. H. Friedman, J. L. Bentley, and R. Finkel, "An algorithm for finding best matches in logarithmic expected time," *ACM Trans. Math. Softw.*, vol. 3, no. 3, pp. 209–226, Sep. 1977.
- [34] S. Zhu and A. Yuille, "Region competition: Unifying snakes, region growing, and Bayes/MDL for multiband image segmentation," *IEEE Trans. Pattern Anal. Mach. Intell.*, vol. 18, no. 9, pp. 884–900, Sep. 1996.
- [35] B. S. Morse, T. S. Yoo, D. T. Chen, P. Rheingans, and K. R. Subramanian, "Interpolating implicit surfaces from scattered surface data using compactly supported radial basis functions," in *Proc. Int. Conf. Shape Modeling Applications*, Washington, DC, 2001, p. 89.
- [36] Y. Ohtake, A. Belyaev, and H.-P. Seidel, "A multi-scale approach to 3D scattered data interpolation with compactly supported basis," in *Proc. Shape Modeling Int.*, Seoul, Korea, 2003, pp. 153–161.
- [37] A. Gelas, Y. Ohtake, T. Kanai, and R. Prost, "Approximation of unorganized point set with composite implicit surface," presented at the IEEE Int. Conf. Image Processing, Atlanta, GA, Oct. 2006.
- [38] X. Huang, N. Paragios, and D. Metaxas, "Shape registration in implicit spaces using information theory and free form informations," *IEEE Trans. Pattern Anal. Mach. Intell.*, 2006, to be published.
- [39] A. Tsai, A. Yezzi, W. Wells, C. Tempany, D. Tucker, A. Fan, W. E. Grimson, and A. Willsky, "A shape-based approach to the segmentation of medical imagery using level sets," *IEEE Trans. Med. Imag.*, vol. 22, pt. 2, pp. 137–154, Feb. 2003.
- [40] P. R. Amestoy, A. Guermouche, J.-Y. L'Excellent, and S. Pralet, "Hybrid scheduling for the parallel solution of linear systems," *Parallel Comput.*, vol. 32, no. 2, pp. 136–156, 2006.
- [41] M. Botsch, D. Bommes, and L. Kobbelt, "Efficient linear system solvers for mesh processing," in *Proc. IMA Conf. Mathematics of Surfaces XI*, 2005, vol. 3604, pp. 62–83.
- [42] S. Osher and R. Fedkiw, "Level set methods: An overview and some recent results," *J. Comput. Phys.*, vol. 169, pp. 463–502, 2001.
- [43] D. Peng, B. Merriman, S. O. H. Zhao, and M. Kang, "A PDE-based fast local level set method," *J. Comput. Phys.*, vol. 155, pp. 410–438, 1999.
- [44] D. Mumford and J. Shah, "Optimal approximation by piecewise smooth functions and associated variational problems," *Commun. Pure Appl. Math.*, vol. 42, pp. 577–685, 1989.
- [45] M. Leventon, W. Grimson, and O. Faugeras, "Statistical shape influence in geodesic active contour," in *Proc. IEEE Int. Conf. Computer Vision and Pattern Recognition*, 2000, pp. 316–323.
- [46] O. Bernard, J. Dhooge, and D. Friboulet, "Segmentation of echocardiographic images based on statistical modelling of the radio-frequency signal," in *Proc. IEEE Int. Symp. Biomedical Imaging*, Arlington, VA, Apr. 2006, pp. 153–156.



Arnaud Gelas (M'06) received the M.S. degree from the Electrical Engineering Department, National Institute for Applied Sciences of Lyon (INSA), Lyon, France, in 2002, and the Ph.D. degree from INSA in 2006.

He is currently a Research Fellow at the Biomedical Imaging Lab, SBIC, A-STAR, Singapore. His research interests include signal processing (reconstruction, interpolation, approximation), image processing (segmentation, registration), and shape modeling (multiresolution mesh, subdivision surface, and implicit surface).



Olivier Bernard received his B.S. degree in electrical engineering from the National Institute for Applied Sciences of Lyon (INSA), Lyon, France, in 2003, and the Ph.D. degree from INSA in 2006.

He is currently in a Postdoctoral Research Fellow position at the Biomedical Imaging Group of Switzerland. His current research interests include signal processing (statistical modeling) and image processing (statistics-based deformable models and level-set based segmentation) applied to the field of echocardiographic imaging.



Denis Friboulet (M'06) was born in Bordeaux, France, in 1961. He received the engineering degree (electrical engineering) and the Ph.D. degree (biomedical engineering) from the National Institute for Applied Sciences of Lyon (INSA) Lyon, France, in 1984 and 1990, respectively.

He is currently a Professor at INSA and a member of the CREATIS-LRMN Laboratory (CNRS #5515 now 5220, INSERM U630, INSA, Claude Bernard Lyon I University of Lyon). His research interests include signal processing (spectral analysis, statistical modeling) and image processing (statistics-based deformable models, level-set based segmentation, motion estimation, and analysis) applied to the field of echocardiographic imaging.



Rémy Prost (M'82) received the doctorate degree in electronics engineering and the "Docteur ès Sciences" degree from Lyon University, Lyon, France, and the National Institute of Applied Sciences (INSA), Lyon, in 1977 and 1987, respectively.

He is currently a Professor in the Department of Electrical Engineering, INSA. Both his teaching and research interests include digital signal processing, inverse problems, image data compression, multiresolution algorithms, wavelets, shape modeling, and 3-D mesh processing. He leads the "Volume (3D) Image Processing" project in the CREATIS-LRMN Laboratory (CNRS #5515 now 5220, INSERM U630, INSA, Claude Bernard Lyon I University of Lyon).